

SMHASH: Anatomy of the Orphan Stream using RR Lyrae stars

David Hendel¹★, Victoria Scowcroft^{2,3}, Kathryn V. Johnston¹, Mark A. Fardal⁴, Roeland P. van der Marel^{4,5}, Sangmo Tony Sohn^{4,5}, Adrian M. Price-Whelan⁶, Rachael L. Beaton⁶, Gurtina Besla⁷, Giuseppe Bono^{8,9}, Maria-Rosa L. Cioni^{10,11}, Gisella Clementini¹², Judith G. Cohen¹³, Michele Fabrizio^{14,9}, Wendy L. Freedman¹⁵, Alessia Garofalo¹⁶, Carl J. Grillmair¹⁷, Nitya Kallivayalil¹⁸, Juna A. Kollmeier³, David R. Law⁴, Barry F. Madore³, Steven R. Majewski¹⁹, Massimo Marengo²⁰, Andrew J. Monson³, Jillian R. Neeley²⁰, David L. Nidever²¹, Grzegorz Pietrzyński²², Mark Seibert³, Branimir Sesar²³, Horace A. Smith²⁴, Igor Soszyński²⁵, Ian B. Thompson³, and Andrezej Udalski²⁵

¹Department of Astronomy, Columbia University, 550 West 120th Street, New York, NY 10027, USA

²Department of Physics, University of Bath, Claverton Down, Bath, BA2 7AY, UK

³Observatories of the Carnegie Institution of Washington, 813 Santa Barbara St., Pasadena, CA 91101, USA

⁴Space Telescope Science Institute, 3700 San Martin Drive, Baltimore, MD 21218, USA

⁵Department of Physics and Astronomy, The Johns Hopkins University, Baltimore, MD 21218, USA

⁶Department of Astrophysical Sciences, Princeton University, 4 Ivy Lane, Princeton, NJ 08544

⁷Steward Observatory, University of Arizona, 933 North Cherry Avenue, Tucson, AZ 85721, USA

Accepted XXX. Received YYY; in original form ZZZ

ABSTRACT

Stellar tidal streams provide an opportunity to study the motion and structure of the disrupting galaxy as well as the gravitational potential of its host. Streams around the Milky Way are especially promising as phase space positions of individual stars will be measured by ongoing or upcoming surveys. Nevertheless, it remains a challenge to accurately assess distances to stars farther than 10 kpc from the Sun, where we have the poorest knowledge of the Galaxy’s mass distribution. To address this we present observations of 32 candidate RR Lyrae stars in the Orphan tidal stream taken as part of the *Spitzer* Merger History and Shape of the Galactic Halo (SMHASH) program. The extremely tight correlation between the periods, luminosities, and metallicities of RR Lyrae variable stars in the *Spitzer* IRAC 3.6 μ m band allows the determination of precise distances to individual stars; the median statistical distance uncertainty to each RR Lyrae star is 2.5%. By fitting orbits in an example potential we obtain an upper limit on the mass of the Milky Way interior to 60 kpc of $5.6_{-1.1}^{+1.2} \times 10^{11} M_{\odot}$, bringing estimates based on the Orphan Stream in line with those using other tracers. The SMHASH data also resolve the stream in line-of-sight depth, allowing a new perspective on the internal structure of the disrupted dwarf galaxy. Comparing with N-body models we find that the progenitor had an initial dark halo mass of approximately $3.2 \times 10^9 M_{\odot}$, placing the Orphan Stream’s progenitor amongst the classical dwarf spheroidals.

Key words: stars: variables: RR Lyrae – Galaxy: kinematics and dynamics – Galaxy: halo – Galaxy: structure

★ E-mail: hendel@astro.columbia.edu

1 INTRODUCTION

Tidal debris structures are striking evidence of hierarchical assembly – the premise that the Milky Way and systems like it have been built over cosmic time through the coalescence of many smaller objects (White & Rees 1978; Johnston et al. 1996; Bullock et al. 2001; Freeman & Bland-Hawthorn 2002). Some of this construction is in the form of major mergers, where two near-equal mass galaxies collide and their stars are redistributed wholesale as the new galaxy violently relaxes. However, in the prevailing Λ – cold dark matter (Λ CDM) model, the vast majority of mergers (by number) are minor (Fakhouri et al. 2010) where one halo, the host, dominates the interaction and a smaller object, the satellite, is dragged inward by dynamical friction and eventually stripped of mass by tidal forces. When the luminous component is disrupted the stars may form a stellar tidal stream or shell, depending on the parameters of the interaction (e.g. Johnston et al. 2008; Amorisco 2015; Hendel & Johnston 2015). The study of tidal features therefore probes the accretion histories of galaxies.

Stellar tidal streams are also key tools for our current understanding of the Milky Way’s gravitational potential. The techniques applied to measure the potential are wide-ranging but commonly a few-parameter potential model is varied in an attempt to match simulations to the available data. Historically, the streams used most often for this purpose are the Sagittarius dwarf galaxy’s stream (Majewski

et al. 2003; Law & Majewski 2010; Gibbons et al. 2014) and various globular cluster streams such as Palomar 5 and GD-1 (Koposov et al. 2010; Küpper et al. 2015; Pearson et al. 2015; Fritz & Kallivayalil 2015; Bovy et al. 2016).

The Orphan tidal stream (Grillmair 2006; Belokurov et al. 2006) has several advantages over the other streams mentioned above. It forms a smooth arc that is significantly longer (detected length of $\approx 108^\circ$, Grillmair et al. 2015), wider ($\sim 2^\circ$, Belokurov et al. 2006), and farther from the Galactic centre (> 50 kpc, Newberg et al. 2010; Sesar et al. 2013) than any of the commonly studied globular cluster streams. Along with its total luminosity ($M_r < -7.5$, Belokurov et al. 2007) and metallicity spread of 0.56 dex (Casey et al. 2013), these characteristics suggest a dwarf spheroidal galaxy as the likely origin, but the progenitor is elusive and possibly nearly completely disrupted by the Galaxy’s tidal field (Grillmair et al. 2015). In contrast to the Sagittarius stream, the Orphan Stream has a uniform appearance and cold velocity structure; the Sagittarius stream is notoriously complex, featuring multiple wraps, bifurcated tails, and several stellar populations with different kinematics (Belokurov et al. 2006; Koposov et al. 2012; Gibbons et al. 2017). The orbital planes of the Orphan and Sagittarius streams are misaligned by $\sim 67^\circ$ (Pawlowski et al. 2012), making the combination of the two an attractive target for multi-stream potential measuring methods (Sanderson et al. 2015; Bovy et al. 2016).

The Orphan Stream also has the advantage of a well-filled horizontal branch resulting in numerous classes of stars that may be used as standard candles for distance estimation, for example the Blue Horizontal Branch (BHB) stars studied by Newberg et al. (2010). Of particular relevance to this work, the Orphan Stream contains a significant population of RR Lyrae stars (RRL), which have been the focus of several recent efforts to improve distance measurement into the Galactic halo (Sesar et al. 2017; Hernitschek et al. 2017). These stars make excellent standard candles using period–luminosity (PL) relations with their near- or mid-infrared magnitudes (Longmore et al. 1986; Bono et al. 2001, 2003; Catelan et al. 2004; Braga et al. 2015). In addition to the advantage of decreased extinction at these longer wavelengths compared to the V band ($A_V/A_{[3.6\mu\text{m}]} > 19$, Cardelli et al. 1989; Indebetouw et al. 2005), the PL relation has also been shown to have a small intrinsic scatter in the infrared (Madore et al. 2013; Neeley et al. 2015). Recently these relations have been extended to include a metallicity component (Neeley et al. 2017) with the effect of further decreasing the uncertainty on individual stars’ absolute magnitudes and thus removing systematic scatter in measured distances for systems with a large range in metallicity, such as the Orphan stream.

The *Spitzer* Merger History And Shape of the Galactic Halo (SMHASH) program builds upon the previous Carnegie RR Lyrae Program (CRRP, Freedman et al. 2012) to leverage these excellent distance indicators and explore a variety of Local Group substructures including five dwarf galaxies (Sagittarius (Gupta et. al, in prep), Sculptor (Garofalo et. al, in prep), Ursa Minor, Carina, and Boötes) along with the Sagittarius and Orphan tidal streams. As we will show, the precision is such that we are able to resolve the three-dimensional structure of the stream, granting special

⁸ Dipartimento di Fisica, Università di Roma Tor Vergata, via Della Ricerca Scientifica 1, I-00133, Roma, Italy

⁹ INAF, Rome Astronomical Observatory, via Frascati 33, I-00040, Monte Porzio Catone, Italy

¹⁰ Leibniz-Institut für Astrophysik Potsdam, An der Sternwarte 16, 14482 Potsdam, Germany

¹¹ University of Hertfordshire, Physics Astronomy and Mathematics, College Lane, Hatfield AL10 9AB, UK

¹² INAF-Osservatorio Astronomico di Bologna, Via Ranzani 1, I - 40127 Bologna, Italy

¹³ Division of Physics, Mathematics and Astronomy, California Institute of Technology, Pasadena, Ca., 91125

¹⁴ Space Science Data Center - ASI, via del Politecnico, s.n.c., I-00133, Roma, Italy

¹⁵ Department of Astronomy & Astrophysics, University of Chicago, 5640 South Ellis Avenue, Chicago, IL 60637, USA

¹⁶ Dipartimento di Fisica e Astronomia, Università di Bologna, Viale Berti Pichat 6/2, I-40127 Bologna, Italy

¹⁷ IPAC, Mail Code 314-6, Caltech, 1200 E. California Blvd., Pasadena, CA 91125

¹⁸ Department of Astronomy, University of Virginia, 530 McCormick Road, Charlottesville, VA 22904, USA

¹⁹ Department of Astronomy, University of Virginia, P.O. Box 400325, Charlottesville, VA 22904-4325, USA

²⁰ Department of Physics and Astronomy, Iowa State University, A313E Zaffarano, Ames, IA 50010

²¹ National Optical Astronomy Observatory, 950 North Cherry Avenue, Tucson, AZ 85719, USA

²² Nicolaus Copernicus Astronomical Center, Polish Academy of Sciences, Bartycka 18, 00-716 Warsaw, Poland

²³ Max Planck Institute for Astronomy, Königstuhl 17, D-69117, Heidelberg, Germany

²⁴ Department of Physics and Astronomy, Michigan State University, East Lansing, MI 48824-2320, USA

²⁵ Warsaw University Observatory, Al. Ujazdowskie 4, 00-478 Warszawa, Poland

access to a system that is in many ways the archetypal minor merger event.

In this work we present *Spitzer Space Telescope* (Werner et al. 2004) Infrared Array Camera (IRAC, Fazio et al. 2004) 3.6 μm magnitudes and inferred distances to 32 candidate Orphan Stream RR Lyrae stars with the principal goal of informing future studies of the Galactic potential and Orphan progenitor. In Section 2 we describe our *Spitzer* photometry and the calculation of apparent magnitudes. Section 3 describes how we derive distances to individual Orphan stream stars. In Section 4 we define a procedure to fit orbits to the RRL and measure bulk properties of the stream; in Section 5 we investigate the extent to which the orbit fits place constraints on the mass of the Milky Way. Section 6 studies the Orphan progenitor and Section 7 concludes.

2 OBSERVATIONS & DATA REDUCTION

2.1 Data Selection

The RR Lyrae stars selected for observation in the SMHASH Orphan program are the 31 ‘high probability’ candidate stream members of Sesar et al. (2013); these stars are all fundamental-mode pulsators (RRab). Also included is one ‘medium probability’ candidate, RR5, because it was measured at large distance despite having a line-of-sight velocity somewhat discrepant with expectations for the Orphan stream given its position. The stars were identified from a compilation of three synoptic sky surveys: the Catalina Real-Time Sky Survey (CRTS, Drake et al. 2009), the Lincoln Near Earth Asteroid Research (LINEAR, Stokes et al. 2000) survey, and the Palomar Transient Factory (PTF, Law et al. 2009; Rau et al. 2009). Sesar et al. (2013) obtained follow-up spectroscopic observations in order to implement a Galactic standard of rest velocity cut as part of their stream membership criteria. All of our targets therefore have uniformly determined metallicity (on the Layden system, Layden 1994) and line-of-sight velocity measurements with uncertainties of 0.15 dex and ~ 15 km/s, respectively. Their catalogue number in Table 1 is in order of decreasing declination, which approximately corresponds to a sequence of increasing apparent magnitude and decreasing Heliocentric distance (see Figure 2 in Sesar et al. 2013).

2.2 *Spitzer* Observations

The mid infrared observations presented here were collected using the Infrared Array Camera (IRAC) on the *Spitzer* Space Telescope as part of the Warm *Spitzer* Cycle 10 between 2014 June 19 and 2015 August 31 (Johnston et al. 2013). Each star was observed in 12 epochs at 3.6 μm only.

The targets selected in the Orphan stream span a wide range in distance, hence cover a significant range in apparent infrared magnitude. In order to achieve a sufficient signal-to-noise ratio on the individual epochs for both the nearest and most distant targets, the stars were divided into two groups based on their distances from Sesar et al. (2013), and their anticipated apparent magnitude from the K-band period-luminosity relation. The closer, brighter targets (with estimated distances less than ~ 40 kpc) were observed at each epoch with five dithered 100 s exposures, with

all 12 epochs approximately uniformly spaced over a single pulsation cycle. The more distant, fainter targets used 25 dithered 100 s exposures to obtain the required S/N ratio. However, given the longer exposure times and the short pulsation cycle of the RRL, it was not possible to schedule all 12 observations within a single pulsation cycle. Instead these observations are spaced non-uniformly over several cycles, with typically 8–10 days between the first and last observation of a given target.

2.3 Photometry

Individual Basic Calibrated Data (BCDs) generated by IRAC pipeline version S19.2 were downloaded from the *Spitzer* Science Center (SSC). Mosaics were created with the SSC-provided software MOPEX (Makovoz & Khan 2005); both individual- and all-epoch (‘master’) mosaics for each field were produced with a 0.6” pixel scale. Point spread function (PSF) photometry was performed using the DAOPHOT/ALLSTAR/ALLFRAME program suite (Stetson 1987, 1994). Further details of the SMHASH photometric procedure are provided in upcoming work (Garofalo et al., in prep).

The Orphan Stream is highly diffuse so crowding from stream members is not important, but we find PSF photometry useful regardless to eliminate any contribution from field stars aligned by chance with the RRL. PSF stars are required to appear in at least 75% of dithers and were chosen from uncrowded stars as determined by visual examination. For each target the PSF made from the epoch 1 mosaic is used on all epochs. Experiments with several stars showed no difference in measured magnitudes when using a PSF made from epoch 1, the master mosaic, or individual PSFs for each epoch.

The photometry was calibrated to the IRAC Vega magnitude system using the standard IRAC aperture correction procedure on the master mosaics, with inner and outer aperture radii of 6 and 14 pixels, respectively. Location corrections were applied to adjust for pixel-to-pixel sensitivity variations using the Warm Mission array location-correction images following the procedure outlined in the Warm *Spitzer* analysis documentation.

2.4 Light Curves & Average Magnitudes

The phase-folded lightcurves for each of our observed stars, using the period and time of maximum brightness determined from the optical data (Table 1), are presented in Figure A1; a subset is shown in Figure 1. Each lightcurve is repeated for 3 phase cycles to highlight the variability. Stars where the telescope’s scheduling resulted in multiple samples of the same point in phase (e.g. RR9, RR18) underscore *Spitzer*’s precision photometric capabilities; field stars have a typical inter-epoch variation of approximately 0.03 mag, somewhat less than their single-epoch photometric uncertainty. Individual 3.6 μm magnitude measurement time series data for each star are provided as an electronic supplement to this article.

A smooth lightcurve is obtained from the observations using the Gaussian Local Estimation (GLOESS, Persson et al. 2004) algorithm. This technique evaluates the mag-

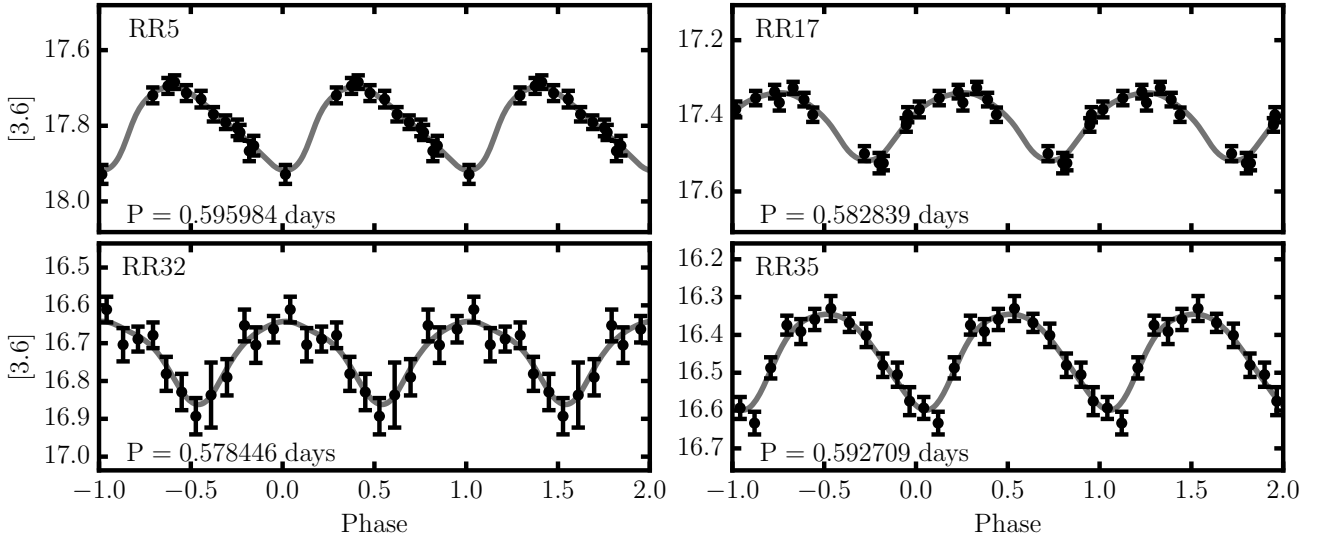


Figure 1. Four example $3.6\mu\text{m}$ SMHASH RRL lightcurves. The remainder are displayed in Figure A1. The infrared lightcurves display a more sinusoidal shape than the sharply peaked and skewed optical lightcurves, as expected. This subset demonstrates the difference in phase coverage between the near and far subsamples; the more distant stars (RR5, RR17) may have substantial gaps resulting from the telescope’s scheduling but often also smaller uncertainties in individual measurements due to the larger number of BCDs per epoch.

nitude at a point in phase by fitting a second-order polynomial to the data, whose contributions to the fit are inversely weighted by the combination of both their statistical uncertainties and Gaussian distance from the point of interest. We use a Gaussian window of width 0.25 (in phase); the flux-averaged magnitude obtained from the fitted curve is not at all sensitive ($\Delta m = 1 - 3 \times 10^{-4}$ mag) to this smoothing length for any reasonable choice. The GLOESS lightcurve is used to determine the time-averaged, intensity-weighted mean magnitude. We compute the uncertainty on this quantity by adding in quadrature the per-star average photometric error and the uncertainty on the mean magnitude of the fitted lightcurve,

$$\sigma_{[3.6]} = \sqrt{\frac{\sum \sigma_i^2}{N^2} + \sigma_{\text{fit}}^2} \quad (1)$$

where N is the number of observations, σ_i is an individual epoch’s photometric uncertainty, and σ_{fit} is the uncertainty on the average magnitude calculated from the GLOESS fit. The latter is dependent on the observing scheme; one can show that the uncertainty on mean magnitude decreases as $1/N$ if the lightcurve is sampled uniformly, in contrast to the slower $1/\sqrt{N}$ drop for data that has been randomly sampled (Freedman et al. 2012). Following the method of Scowcroft et al. (2011), we take advantage of this property where appropriate and compute $\sigma_{\text{fit}} = A/(N\sqrt{12})$ for the brighter, uniformly sampled stars and $\sigma_{\text{fit}} = A/(\sqrt{12}N)$ for the fainter, nonuniformly observed subset, where A is the amplitude of the GLOESS lightcurve. Table 1 compiles the SMHASH mean magnitudes calculated in this way along with the archival data.

2.5 Membership and contamination

One of the principal difficulties in the study of halo substructure is separating tracers belonging to the object of interest from the background of halo objects of the same type. While the surveys contributing to the Orphan RRL catalogue are expected to be $> 95\%$ complete, partitioning the objects into members and contaminants is key to drawing any conclusions from them. For this study of Orphan in particular, the issue is further complicated by one of Sagittarius’ tails crossing the survey area around Galactic longitude $l \sim 200^\circ$; fortunately the Sagittarius debris is offset from the Orphan Stream in heliocentric radial velocity by $\sim 200 \text{ km s}^{-1}$ in this part of the sky (e.g. Law et al. 2005). This section discusses several heuristics that may be used to differentiate individual populations.

A typical way of separating stellar systems is identifying characteristic patterns in their chemical abundances left by their star formation histories. Unfortunately, the SMHASH sample has a mean $[\text{Fe}/\text{H}]$ of -2.1 dex and a dispersion of about 0.25 dex, which is not distinguishable from either the sample of stars in Sesar et al. (2013) whose kinematics are inconsistent with stream membership or RR Lyrae stars more generally in the smooth halo (mean $[\text{Fe}/\text{H}] \sim -1.7$, $\sigma \sim 0.3$, Drake et al. 2013). The mean metallicity can be used, however, to estimate how many Orphan stars we should expect in the survey area. Using the universal dwarf galaxy luminosity–metallicity relation obtained by Kirby et al. (2013) and the Orphan Stream K-giant metallicity of -1.63 ± 0.19 from Casey et al. (2013) (which should be more representative than the metal-poor RRL), we calculate that the progenitor should have had a luminosity $L_V \sim 1.6 \times 10^6 L_\odot$. Sanderson (2016) found that the quantity $\log_{10} N_{\text{RRLy}}/L_\odot$ is linear in metallicity with a scatter of 0.64 dex, which, when combined with the luminosity estimate, implies that the Orphan debris system has of order

Table 1. Distances and Light Curve Parameters of SMHASH Orphan RR Lyrae stars

ID	R.A. (J2000)	Decl. (J2000)	Period (days)	HJD ₀ ^a (days)	[3.6] mag ^b mag	[3.6] amp. mag	A _[3.6] ^c mag	[Fe/H]	Helio. Distance kpc
RR4	142.596437	49.440867	0.677648	54265.667221	17.39 ± 0.01	0.158	0.003	-2.32	44.04 ± 1.06
RR5	139.486634	49.043981	0.595984	54508.734151	17.79 ± 0.02	0.223	0.002	-2.05	48.88 ± 1.21
RR6	143.840446	47.091109	0.530818	55887.972840	17.94 ± 0.03	0.341	0.002	-2.37	50.91 ± 1.36
RR7	141.771831	46.359489	0.639017	55590.054047	17.67 ± 0.02	0.257	0.003	-1.94	47.27 ± 1.19
RR9	144.271648	42.603354	0.567199	54913.653005	17.63 ± 0.02	0.219	0.002	-2.08	44.36 ± 1.10
RR10	142.541300	42.570500	0.649151	54157.679811	17.70 ± 0.02	0.211	0.002	-2.53	50.62 ± 1.26
RR11	144.881448	41.439236	0.624166	56271.888900	17.39 ± 0.02	0.200	0.002	-2.56	43.26 ± 1.07
RR12	146.057798	40.220714	0.711552	56334.821312	17.21 ± 0.02	0.228	0.003	-2.35	41.61 ± 1.04
RR13	143.482581	39.134007	0.527853	54415.904058	17.73 ± 0.02	0.186	0.002	-2.22	45.47 ± 1.11
RR14	143.913227	38.853250	0.504139	53789.793479	18.00 ± 0.01	0.151	0.002	-2.36	51.21 ± 1.23
RR15	146.447585	37.553258	0.624026	54913.654037	17.00 ± 0.02	0.183	0.002	-2.14	34.87 ± 0.85
RR16	148.586324	37.191956	0.573213	54941.722401	17.52 ± 0.01	0.151	0.002	-2.18	42.81 ± 1.03
RR17	142.909363	37.002696	0.582839	55598.766679	17.41 ± 0.02	0.179	0.002	-2.73	43.01 ± 1.05
RR18	146.008547	36.265846	0.594436	53789.812373	17.30 ± 0.01	0.163	0.002	-2.27	39.53 ± 0.96
RR19 ^d	146.390649	35.795310	0.755026	52722.727848	16.85 ± 0.01	0.051	0.002	-1.96	34.92 ± 0.81
RR23	150.579833	26.598017	0.573755	53078.770191	16.95 ± 0.03	0.313	0.004	-2.42	33.61 ± 0.89
RR24	150.243511	25.826153	0.708142	54476.844880	16.63 ± 0.01	0.158	0.005	-2.14	31.17 ± 0.75
RR25	150.647213	25.247547	0.542891	54539.656204	16.87 ± 0.02	0.202	0.005	-2.12	30.83 ± 0.76
RR26	151.892507	24.831492	0.620861	53788.855568	16.83 ± 0.02	0.231	0.006	-2.09	32.09 ± 0.80
RR27	150.544334	24.257983	0.604737	54595.657970	16.82 ± 0.02	0.267	0.005	-1.86	30.89 ± 0.79
RR29	153.996368	19.222735	0.645174	53816.785913	16.50 ± 0.02	0.234	0.004	-2.00	27.84 ± 0.70
RR30	153.698975	19.125864	0.630652	54149.788097	16.35 ± 0.02	0.175	0.005	-2.09	25.86 ± 0.63
RR31	154.238008	18.790623	0.508603	52648.880186	16.33 ± 0.02	0.235	0.005	-1.97	23.06 ± 0.58
RR32	154.824925	18.226018	0.578446	54084.925828	16.73 ± 0.02	0.220	0.005	-1.61	28.42 ± 0.70
RR33	154.469145	17.427796	0.575995	54207.717695	16.84 ± 0.02	0.219	0.005	-1.75	30.16 ± 0.75
RR34	154.295002	17.131504	0.513222	53706.970133	16.66 ± 0.02	0.253	0.005	-1.88	26.71 ± 0.67
RR35	156.791313	15.992450	0.592709	54175.771290	16.45 ± 0.02	0.254	0.005	-2.32	26.84 ± 0.68
RR39	158.493827	9.235715	0.554073	53851.699888	16.34 ± 0.02	0.219	0.004	-2.00	24.13 ± 0.60
RR43	160.996538	3.565153	0.618892	53710.968168	16.64 ± 0.02	0.231	0.006	-2.31	29.87 ± 0.75
RR46	161.045184	0.876656	0.591287	54535.792607	16.70 ± 0.03	0.295	0.007	-1.58	28.26 ± 0.73
RR47	161.622376	0.491299	0.463190	54180.766355	16.34 ± 0.02	0.263	0.006	-1.50	21.31 ± 0.54
RR49	162.349340	-2.609458	0.523622	53054.827672	16.30 ± 0.02	0.245	0.006	-2.02	23.05 ± 0.58

^a Reduced Heliocentric Julian Date of maximum brightness (HJD – 2400000)^b Extinction-corrected, flux-averaged 3.6 μ m apparent magnitude from GLOESS fit (Section 2.4)^c 3.6 μ m extinction from the Schlafly & Finkbeiner (2011) dust map, calculated by <http://irsa.ipac.caltech.edu/applications/DUST/>^d RR19 is likely not an RR Lyrae star (or a member of the Orphan Stream) but we include it here for completeness.

100 RRL – with an uncertainty of ~ 0.7 dex. Given that our precursor catalogues likely only cover one tail of the stream and that there are approximately 20 stars without spectra that Sesar et al. (2013) find are consistent with the stream’s distance, we conclude that the observed RRL population is appropriate given the probable progenitor.

Next we consider the contribution of a principal contaminant population – the smooth stellar halo. For some time it has been known that the number density of halo RR Lyrae stars sharply decreases at a Galactocentric distance of approximately 25 kpc (Saha 1985). More recent studies have shown that the power law index of this decline is $n = -4.5$ or greater (Keller et al. 2008; Watkins et al. 2009; Sesar et al. 2010; Cohen et al. 2017). This is a significant advantage for studies of substructures beyond about 30 kpc as contaminants from the smooth component become almost negligible. For the case of the SMHASH Orphan footprint in particular, using the latest density normalization from Sesar et al. (2010), we expect only about 4 halo interlopers between 30 and 40 kpc and only 2 between 40 and 50 kpc; it is unlikely with such small numbers that they would also match the ra-

dial velocity trend of the stream. The catalogue star RR5 is marked as a medium-probability member for precisely this reason – distant at 49 kpc but discrepant in radial velocity by 100 km s⁻¹.

There is also a subset of RRL that we do not expect to find as part of the Orphan Stream: high amplitude short period (HASP) RRab stars. These are fundamental mode pulsators that have large amplitudes, $A_V \geq 0.75$ mag, but periods less than approximately 0.48 days. RR Lyrae variables in dwarf spheroidal galaxies do not populate this part of the period-amplitude plane, possibly because their metallicity evolution is too slow to produce a component both old enough and metal rich enough to pulsate in this range (Bersier & Wood 2002; Fiorentino et al. 2015). The smooth halo does, however, contain stars in the HASP parameter space at the several percent level and therefore such stars are likely contaminates. Amongst the SMHASH Orphan sample only RR47 meets the HASP criteria; it is also at the smallest distance from the Galactic centre, where the smooth halo is more dominant as described above. Since it has not yet been proven that the Orphan Stream’s progenitor was a dwarf

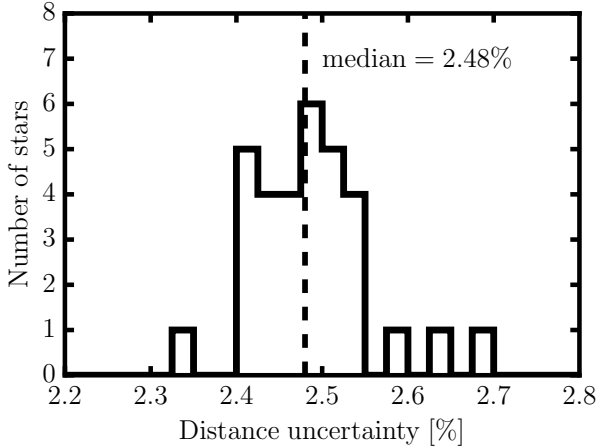


Figure 2. Relative heliocentric distance uncertainties σ_d/d for the SMHASH Orphan RRL. The median uncertainty is indicated by the vertical dashed line. The scatter in the period–luminosity–metallicity relation and the uncertainty on apparent magnitudes each contribute $\sim 1\%$, with the uncertainty in the star’s individual metallicities providing the remainder.

spheroidal galaxy we do not exclude RR47 from the following dynamical analysis but note that the conclusions are not substantively changed if it is omitted.

Finally, we can use our $3.6\mu\text{m}$ data to identify non-RRL contaminants. Examination of the lightcurve for RR19 leads us to believe that it is not, in fact, an RRL. This star was observed over a single presumed period but there is no evidence of coherent variability. The optical lightcurve from the LINEAR, folded at the catalogue period, shows what might best be described as ‘bursty’ variability, which is also inconsistent with being an RRL. Investigating this further, we performed our own period search on the LINEAR data and found no significant periods consistent with being an RRL for this star. We posit that this may simply be a false positive in the database. RR19 is therefore excluded from the rest of our analysis, however we include it in Table 1 and Figure A1 for completeness.

3 DISTANCES TO THE ORPHAN RR LYRAE STARS

Distances to each Orphan RRL are determined using the (RRab–only) theoretical period–luminosity–metallicity (PLZ) relation of Neeley et al. (2017). They derived the PLZ using nonlinear, time–dependent convective hydrodynamical models of RR Lyrae variables with a range of metal abundances. They found that fitting those models with a simple period–luminosity relation results in an ‘intrinsic’ scatter of ~ 0.13 mag, whereas including a metallicity term reduces the scatter to ~ 0.035 mag. The absolute magnitude in IRAC $3.6\mu\text{m}$ is given by

$$M_{[3.6]} = 2.276(\pm 0.021)\log(P) + 0.184(\pm 0.004)[\text{Fe}/\text{H}] - 0.786(\pm 0.007). \quad (2)$$

We fully propagate all sources of uncertainty, including

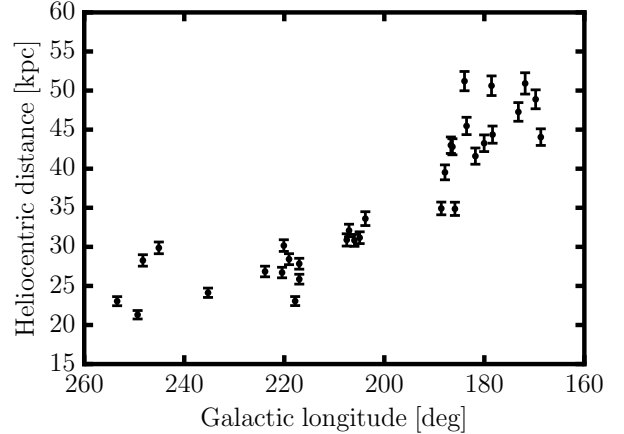


Figure 3. Measured heliocentric distances of the SMHASH Orphan RR Lyrae stars as a function of Galactic longitude. At large distances around 50 kpc the stream is approximately 8 kpc deep.

those from the photometry, the lightcurve fit, the constants in the PLZ relation including its intrinsic scatter, the measured metallicities, and the extinction in this band, $A_{[3.6]}$. The latter is calculated from the Schlafly & Finkbeiner (2011) dust map¹. Because the extinction is very low, ~ 0.005 mag, the entire value is adopted as the uncertainty on extinction. This conservative choice negligibly affects the resultant uncertainty on $M_{[3.6]}$.

The SMHASH Orphan Stream sample’s distance uncertainty distribution is shown in Figure 2. The median relative distance uncertainty is a mere 2.5%. For comparison, end–mission parallax distances to RR Lyrae stars obtained by *Gaia* are expected to have 10% uncertainties for stars at just 6 kpc (Price–Whelan & Johnston 2013), while we are measuring stars at 51 kpc.

It is interesting to consider which, if any, of the observational uncertainties most strongly limit the precision of SMHASH distances. An elementary analysis of the error budget suggest that the metallicity uncertainty and Z term slope contribute 0.5%, the photometric and fit uncertainties contribute 0.9%, and the intrinsic scatter, period slope and zero point are responsible for 1.1% of the 2.5% relative uncertainty. The heliocentric distances derived for each RRL using the Neeley et al. (2017) PLZ relation are given in Table 1.

Figure 3 shows the RRLs’ heliocentric distances as a function of Galactic longitude. We trace the stream to approximately 51 kpc. This figure makes it apparent that the Orphan Stream is not ‘thin’ at large distances; near $l = 180^\circ$ the stream is approximately 10 kpc deep from a heliocentric perspective. In Section 6 we will argue that this depth contains information about the stream’s progenitor. Overall, the SMHASH distances are in good agreement ($\sim 1\sigma$) with the previous work of Sesar et al. (2013), who used an optical luminosity–metallicity relation (Cacciari & Clementini 2003) to obtain distances to these same RR Lyrae stars. On average we find that our measurements are 5% larger than

¹ evaluated using

<http://irsa.ipac.caltech.edu/applications/DUST/>

the values of Sesar et al. (2013); notably, however, we find that their two most remote stars are ~ 5 kpc closer, reducing the maximum heliocentric distance of the stream from about 55 to about 51 kpc.

4 PROPERTIES OF THE ORPHAN STREAM

In the following we assume that all of the SMHASH RR Lyrae stars do indeed belong to the Orphan Stream, and so use them to outline its path and properties. We do this by (i) assuming a form for a galactic potential; (ii) finding the parameters of the potential and the orbit within that potential that best fits the centroid of the RRL positions in their measured dimensions; and (iii) measuring the dispersions in line-of-sight distance, angular size on the sky, and radial velocity about this best-fitting orbit.

Note that, since orbits of debris stars are offset from the progenitor satellite orbit (Johnston 1998; Helmi & White 1999) we expect this approach to provide *biased* estimates of the true potential parameters and orbit of the progenitor (see Eyre & Binney 2011; Sanders & Binney 2013; Lux et al. 2013, as well as our own exploration in Section 5.2). We nevertheless choose to fit orbits and potentials rather than – for example – a polynomial to the path since this allows us to both measure the structure of the stream via its depth and compare our results to the prior work of Newberg et al. (2010). The reader is cautioned that the ‘best-fitting’ potential and orbit are not expected to correspond exactly to the potential of the Milky Way or the orbit of the progenitor. However, the dispersion about the path outlined by the stream *do* contain clues to the nature of the progenitor (see Section 6).

4.1 Fitting method

To fit an orbit to our RRL we use `emcee` (Foreman-Mackey et al. 2013), a Python implementation of an affine-invariant ensemble sampler for a Markov Chain Monte Carlo (MCMC) algorithm (Goodman & Weare 2010), to draw samples from the posterior probability density of the model parameters. This method is similar to that of Koposov et al. (2010), Sesar et al. (2015) and Price-Whelan et al. (2016).

4.1.1 Potential model

The Milky Way potential is represented as three smooth, static components: a Miyamoto & Nagai (1975) disk, a Hernquist (Hernquist 1990) bulge, and a spherical logarithmic halo, defined as

$$\Phi_{\text{disk}} = -\alpha \frac{GM_{\text{disk}}}{\sqrt{R^2 + (a + \sqrt{z^2 + b^2})^2}} \quad (3)$$

$$\Phi_{\text{sphere}} = \frac{GM_{\text{sphere}}}{r + c} \quad (4)$$

$$\Phi_{\text{halo}} = v_{\text{halo}}^2 \ln(R^2 + z^2 + r_h^2) \quad (5)$$

with component masses $M_{\text{sphere}} = 3.4 \times 10^{10} M_{\odot}$ and $M_{\text{disk}} =$

$1 \times 10^{11} M_{\odot}$, disk scale length $a = 6.5$ kpc, disk scale height $b = 0.26$ kpc, bulge core radius $c = 0.7$ kpc, and halo scale radius $r_h = 12$ kpc; R and z are the cylindrical coordinates and r is the spherical radius. We fix the solar distance to the Galactic centre as $R_0 = 8$ kpc (consistent with previous work, but also measurements e.g. Gillessen et al. 2009) and the peculiar velocity of the Sun $(U, V, W)_{\odot} = (11.1, 12.24, 7.25)$ km s $^{-1}$ (Schönrich et al. 2010). In the orbit fitting algorithm the only potential parameter allowed to vary is the dark matter halo’s scale velocity v_{halo} , with r_h chosen such that the total potential’s circular velocity at the solar position is 220 km s $^{-1}$ (e.g. Bovy et al. 2012). These parameters are chosen to match Model 5 of Newberg et al. (2010) (their best-fitting model with a logarithmic halo) which in turn is an implementation of the best-fitting spherical model of Law et al. (2005) except that the halo scale velocity is allowed to vary. We note that the constraint on the circular velocity precludes us from fitting precisely Newberg et al. (2010)’s Model 5 since that potential’s circular velocity at the solar position is only 207 km s $^{-1}$.

4.2 Model parameters

We wish to find the phase space coordinates of the initial condition $\mathbf{x}^0 = (l, b, DM, \mu_l, \mu_b, v_r)^0$ for the orbit that best reproduces the observed sky positions l_i, b_i , heliocentric radial velocities $v_{r,i}$ and distance moduli DM_i of the RRL given their uncertainties $\sigma_{v_{r,i}}, \sigma_{DM_i}$. The sky coordinates are assumed perfectly known and are transformed to the Orphan frame Λ, B defined in Newberg et al. (2010), a heliocentric spherical coordinate system in which the Orphan Stream lies approximately on the equator. The rotation between Galactic coordinates and the Orphan coordinates is defined by the Euler angles $(\phi, \theta, \psi) = (128.79^\circ, 54.39^\circ, 90.70^\circ)$. We set $l^0 = 200^\circ$ without interesting loss of generality.

Because tidal streams are generated with orbital parameters somewhat offset from the progenitor galaxy and with some intrinsic scatter (cf. Hendel & Johnston 2015, and references therein) we also include additional model parameters $\delta = (\delta_B, \delta_{v_r}, \delta_{DM})$ to account for the average dispersions in the observational coordinates. We neglect the fact that each of these dispersions will vary along the stream. Besides representing the physical width, velocity dispersion, and depth of the stream, they serve to deter over-fitting in coordinates where δ/σ is large. The last parameter is the halo scale velocity v_{halo} . The full parameter set is then $\theta = ((b, DM, \mu_l, \mu_b, v_r)^0, (\delta_B, \delta_{v_r}, \delta_{DM}), v_{\text{halo}})$. Orbits were integrated using a symplectic leapfrog integrator as implemented in the Gala package (Price-Whelan 2017).

The MCMC algorithm uses 144 walkers to explore this nine-dimensional parameter space. After running for a burn-in period of 1,000 steps the sampler is restarted and run for an additional 10,000 steps. Since the autocorrelation time for each walker is ~ 50 steps in all dimensions, only every 100th sample is taken from the chains to be included in the posterior. This ensures that each is a nearly independent sample from the posterior distribution. The autocorrelation time does not change substantially after the burn-in period, indicating that the sampling has converged.

4.2.1 Likelihood

We assume that our data are independent and that the uncertainties in each coordinate are normally distributed. Thus the joint likelihood is the product of the likelihoods in each coordinate, which are

$$p(B_i|\Lambda_i, \theta) = \mathcal{N}(B_i|B^{\text{model}}(\Lambda_i), \delta_B^2) \quad (6)$$

$$p(v_{r_i}|\Lambda_i, \theta) = \mathcal{N}(v_{r_i}|v_r^{\text{model}}(\Lambda_i), \sigma_{v_r}^2 + \delta_{v_r}^2) \quad (7)$$

$$p(DM_i|\Lambda_i, \theta) = \mathcal{N}(DM_i|DM^{\text{model}}(\Lambda_i), \sigma_{DM}^2 + \delta_{DM}^2) \quad (8)$$

where B^{model} , v_r^{model} , and DM^{model} are interpolated from the model orbit integrated using the initial conditions in θ and \mathcal{N} is the normal distribution

$$\mathcal{N}(x|\mu, \sigma^2) = \frac{1}{\sqrt{2\pi\sigma^2}} \exp\left(-\frac{(x-\mu)^2}{2\sigma^2}\right) \quad (9)$$

with μ as its mean and σ its standard deviation.

4.2.2 Priors

We implement priors on Galactic latitude and distance modulus that are uniform in Cartesian space; for the former this is uniform in $\cos(b)$, while the latter is

$$p(\text{DM}) \propto 10^{\frac{2}{5}\text{DM}+2}. \quad (10)$$

Using the notation $\mathcal{U}(f, g)$ for the uniform distribution with endpoints f and g , we place an uninformative prior on Heliocentric radial velocity as

$$p(v_r) = \mathcal{U}(50, 300) \text{ km s}^{-1}. \quad (11)$$

The dispersions δ_i are required to be positive to prevent a physically equivalent but bimodal posterior that hampers the walkers' convergence. We use logarithmic (scale-invariant) priors for these parameters,

$$p(\delta_i) \propto \delta_i^{-1} \quad (12)$$

The halo scale velocity v_{halo} must be greater than about 68 km s⁻¹ to maintain a circular speed at the solar radius of 220 km s⁻¹ given our choices for the other parameters. It is therefore constrained by

$$p(v_{\text{halo}}) = \mathcal{U}(68, 200) \text{ km s}^{-1}. \quad (13)$$

Finally, we consider the two phase space dimensions that are unobserved for individual RRL: their proper motions. Since we cannot compare them to a prior on a star-by-star basis, we instead use the value for the model orbit where it crosses $l = 199.7796^\circ$. This position is specifically chosen to correspond to the location of *Hubble Space Telescope*–based proper motions of Orphan Stream stars (Sohn et al. 2016). We consider two cases: first wide, uninformative priors

$$p(\mu_l \cos b) = \mathcal{U}(-5, 5) \text{ mas yr}^{-1} \quad (14)$$

$$p(\mu_b) = \mathcal{U}(-5, 5) \text{ mas yr}^{-1}, \quad (15)$$

and then those based on the *Hubble* observations

$$p(\mu_l \cos b) = \mathcal{N}(0.211, 0.05^2) \text{ mas yr}^{-1} \quad (16)$$

$$p(\mu_b) = \mathcal{N}(-0.774, 0.05^2) \text{ mas yr}^{-1}. \quad (17)$$

In the following we will refer to the former as ‘without’ a proper motion prior for conciseness.

4.3 Centroid of the Orphan Stream

Figure 4 shows a corner plot displaying projections of the orbit fitting's posterior distribution, in the case of the uniform proper motion priors. The median value of the samples in each parameter, along with uncertainties computed as the 16th and 84th percentiles (the 68% credible interval), are summarized in Table 2. We confirm that the orbit is prograde with respect to the Milky Way's rotation. Even if the walkers are restricted to only exploring the space of retrograde orbits, there are no local maxima to compare to the prograde fit shown here. If the overdensity detected by Grillmair et al. (2015) is indeed the nearly-disrupted progenitor then this direction of motion makes the SMHASH RR Lyrae stars part of the leading tidal tail. The median distance modulus of 17.68 mag corresponds to a heliocentric distance of 34.2 kpc; this is approximately 150 pc more distant than Newberg et al. (2010)'s Model 5 orbit at the same longitude, however they are compatible within their respective uncertainties.

Focusing on each of the 2d histograms in Figure 4 in turn, one sees that the fit parameters have minimal covariance with few exceptions: the proper motions $\mu_l \cos(b)$ with μ_b , v_{halo} with $\mu_l \cos(b)$, and to a lesser extent v_{halo} with μ_b and with v_r . Note that the stream's Galactic latitude varies by only a few degrees in the area of our observations. It is no coincidence that the velocity components covary with the scale of the halo; it represents the need for additional kinetic energy to reach the same Galactocentric radius in a deeper potential. This means that currently available proper motion measurements can be highly informative when applied in combination with SMHASH's precision distances. For example, the 68% credible interval of the marginalized posterior for $\mu_l \cos(b)$ spans almost 0.2 mas yr⁻¹ while the uncertainty on the same quantity computed from the measurement of Sohn et al. (2016) is ≈ 0.05 mas yr⁻¹.

4.4 Stream fitting with six-dimensional constraints

Figure 5 illustrates the effect of the precise proper motion constraints on the final positions of the MCMC walkers on the three most affected dimensions – $\mu_l \cos(b)$, μ_b , and v_{halo} . On the left we highlight these quantities in the uninformative case; here we find $\mu_l \cos(b)$ and μ_b from the best-fitting orbits are $\sim 2\sigma$ discrepant with the measured value. The strength of the Sohn et al. (2016) priors are such that when applied to the walkers (on the right) the means of the marginalized posterior distributions are shifted wholesale, making the two nearly disjoint. The halo scale parameter is dragged to significantly higher values, as one would naively expect based on the covariance with $\mu_l \cos(b)$.

The marginalized posterior of v_{halo} can be directly converted into a distribution of enclosed masses at any given radius; we choose 60 kpc for convenient comparison with literature values. The results of this transformation are shown

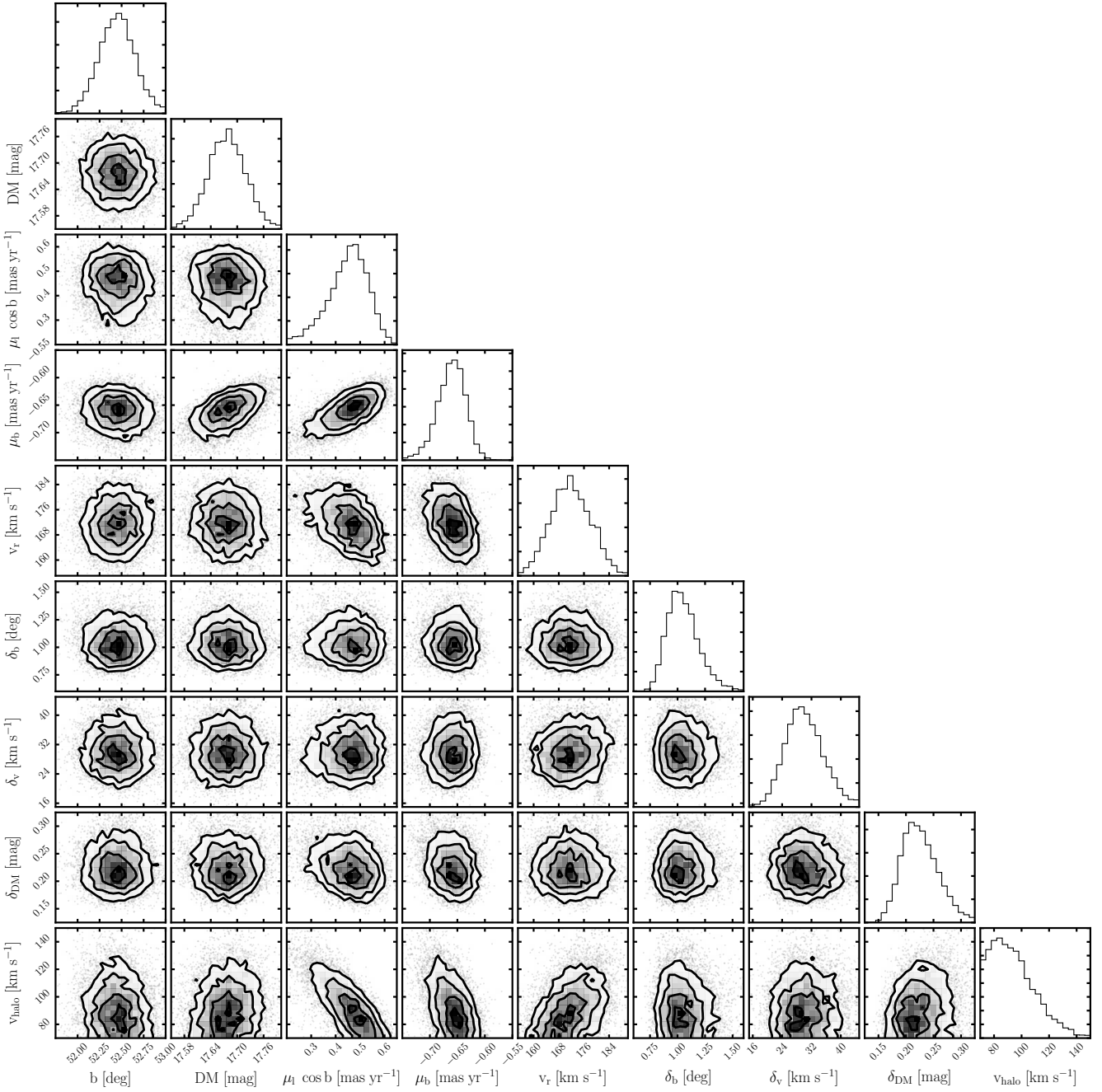


Figure 4. Corner plot (Foreman-Mackey 2016) displaying the posterior distributions of the MCMC walkers for the case of uninformative proper motion priors. Contour plots show the posterior marginalized over the other seven dimensions; histograms are marginalized over all but one. In general there is little covariance between parameters with the notable exceptions of $\mu_1 \cos b$ with μ_b and the velocity components with v_{halo} . This suggests that precise proper motion measurements will add significantly to the constraint on enclosed mass.

in Figure 6, both without (in blue hatch) and with (in red) the observed proper motions as a prior. The difference between them is dramatic: the latter’s median value is 64 per cent larger than the former.

A selection of orbits generated from randomly chosen samples of the posteriors are shown in Figure 7. The left (right) panels show the results without (with) including informative proper motion priors. Plotted from top to bottom are projections in the three observational coordinates (Galactic latitude, radial velocity, and distance) as a func-

tion of Galactic longitude. Both sets of samples capture the path of the stream over most of the survey area. Individual orbits diverge somewhat around $l \lesssim 170^\circ$ where the depth in line-of-sight distance is large. Both sets of orbits seem to systematically overestimate the Heliocentric radial velocity of stars above $l \approx 250^\circ$, however individual stars are only offset by $\sim 1 \delta_i$. Including the Sohn et al. (2016) measurement slightly improves the match to the data in b and v_r but causes the distance to the far end of the stream to be underestimated. This is problematic because the leading arm

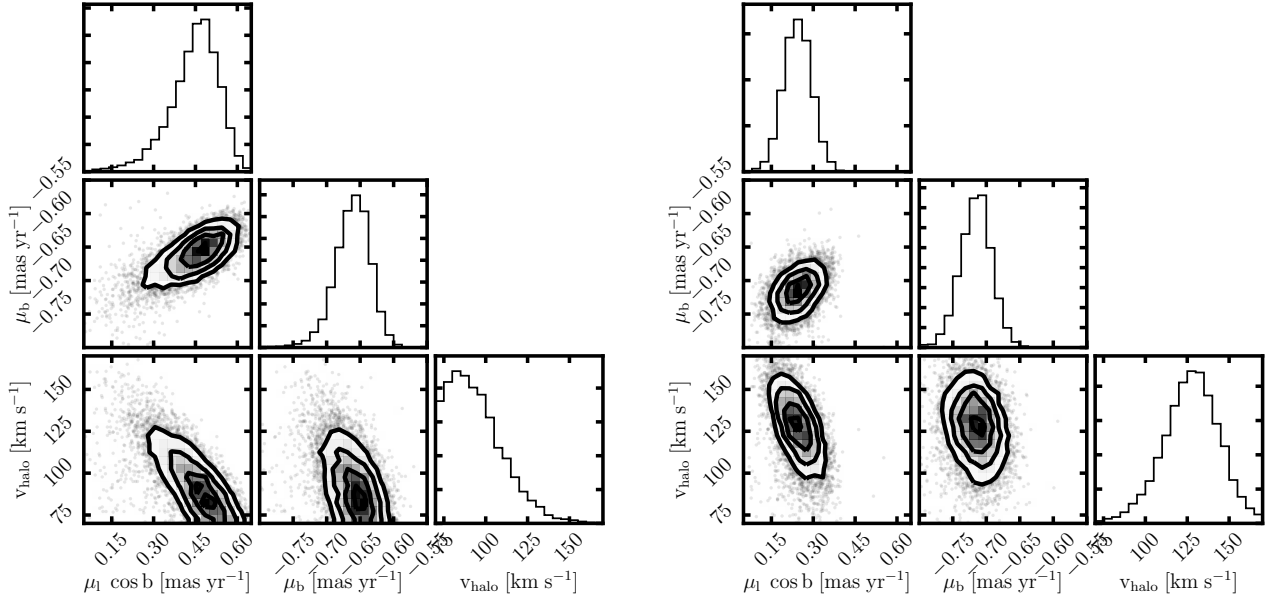


Figure 5. Corner plot displaying the marginalized posterior distributions for the model parameters $\mu_l \cos(b)$, μ_b , and v_{halo} along with their covariances. Left: uniform prior on $\mu_l \cos(b)$ and μ_b . Right: result when otherwise identical chains are run with the additional priors $p(\mu_l \cos(b)) = \mathcal{N}(0.211, 0.05^2)$, $p(\mu_b) = \mathcal{N}(-0.774, 0.05^2)$. Due to the covariance between the proper motions and the halo scale velocity, these priors result in a median v_{halo} that corresponds to a halo 64% more massive than the uniform case.

Parameter	Without PM prior	With PM prior
l [deg]	199.7796	199.7796
b [deg]	$52.45^{+0.21}_{-0.21}$	$52.46^{+0.23}_{-0.21}$
DM [mag]	$17.68^{+0.04}_{-0.04}$	$17.66^{+0.05}_{-0.05}$
$\mu_l \cos(b)$ [mas yr $^{-1}$]	$0.456^{+0.071}_{-0.096}$	$0.244^{+0.049}_{-0.051}$
μ_b [mas yr $^{-1}$]	$-0.660^{+0.023}_{-0.028}$	$-0.715^{+0.022}_{-0.024}$
v_r [km s $^{-1}$]	$171.7^{+6.9}_{-6.3}$	$176.2^{+6.5}_{-6.8}$
δ_B [deg]	$1.042^{+0.168}_{-0.129}$	$1.039^{+0.175}_{-0.129}$
δ_v [km s $^{-1}$]	$29.86^{+5.72}_{-4.82}$	$29.61^{+5.81}_{-4.94}$
δ_{DM} [mag]	$0.224^{+0.040}_{-0.030}$	$0.258^{+0.046}_{-0.036}$
v_{halo} [km s $^{-1}$]	92^{+19}_{-14}	128^{+16}_{-17}
$M(60 \text{ kpc}) [10^{11} M_{\odot}]$	$3.4^{+1.1}_{-0.65}$	$5.6^{+1.2}_{-1.1}$

Table 2. Median and 68% credible intervals of parameters in the posterior distribution resulting from orbit fitting to the SMHASH data, with and without including the observational proper motion constraints. The fixed Galactic longitude value used for the initial condition is included for completeness, along with the mass enclosed at 60 kpc implied by the v_{halo} distribution.

of the stream is made up of stars with lower specific energy than the progenitor and are expected to be *interior* to its orbit. We interpret this mismatch as evidence that the 1-parameter potential model used here is not flexible enough

to recover the full phase space structure of the stream. In the N-body models described below there is no offset between fitted orbits and selected particles at the 0.05 mas yr $^{-1}$ level.

4.5 The Solar circular velocity as measured from the Orphan Stream

To the extent that a stream follows an orbit, the proper motion of member stars perpendicular to the stream should be zero. Any observed perpendicular proper motion is therefore a measure of the solar reflex (c.f. Carlin et al. 2012). The *Hubble* proper motion measurement and the SMHASH distance distribution posterior can be combined at the longitude of the Sohn et al. (2016) Orphan F1 field to estimate the solar motion.

We define a new coordinates system relative to the Orphan coordinates of Newberg et al. (2010) with axes that point into the plane of the sky, parallel to the stream, and perpendicular to the stream. The unit vector perpendicular to the stream points in the direction (in Orphan coordinates) $\hat{n} = (0.62619, 0.50664, 0.59261)$. In this direction, the marginalized posterior derived using the *Hubble* proper motion priors approximates a Gaussian with mean 136.5 km s $^{-1}$ and dispersion 9.1 km s $^{-1}$. If we assume that the solar peculiar velocity relative to the local standard of rest (LSR) is known from Schönrich et al. (2010), then this implies that the azimuthal velocity of the LSR (which equals the circular velocity if the disk is circular) is $v_y = 235 \pm 16$ km s $^{-1}$. This result is consistent with both the traditional IAU value of 220 km s $^{-1}$ as well as some more recent methods that give somewhat larger results (e.g. McMillan 2011; Bovy et al. 2012). While this new measurement does not help to resolve the controversy on the exact value of the solar motion, it does

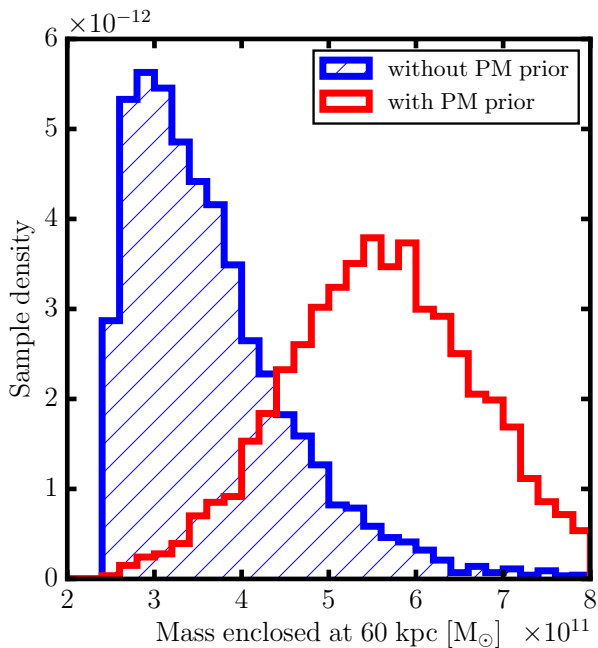


Figure 6. Milky Way mass enclosed at 60 kpc, calculated from the scale velocities v_{halo} of the samples. Including the proper motion prior significantly increases the median value, from $3.4 \times 10^{11} M_{\odot}$ (in blue hatch) to $5.6 \times 10^{11} M_{\odot}$ (in red)

provide an independent consistency check on the SMHASH distances.

5 IMPLICATIONS FOR THE MILKY WAY'S MASS

Orbit fitting is known to introduce systematic biases in potential measures (Eyre & Binney 2011; Sanders & Binney 2013; Lux et al. 2013). To investigate what effect this might have for the specific case of the Orphan Stream, we have created N-body models of the stream and ‘observed’ them in such a way as to recreate the SMHASH dataset. We then apply an identical orbit fitting technique and compare with the simulation inputs. This method allows us to contextualize the results of our RRL observations in terms of the direction and size of systematic biases as well as compare them with earlier results.

Previous measurement of the Milky Way’s mass using the Orphan Stream found that the best-fitting halo was a factor of ~ 2 less massive inside 60 kpc ($2.74 \times 10^{11} M_{\odot}$, Newberg et al. 2010) than contemporary models using other techniques, such as fitting Sagittarius Stream data ($4.7 \times 10^{11} M_{\odot}$, Law et al. 2005) or the velocity distribution of field BHB stars ($4.0 \times 10^{11} M_{\odot}$, Xue et al. 2008). A complete summary of mass estimates is outside the scope of this work; the review of Bland-Hawthorn & Gerhard (2016) provides an overview. However, the Newberg et al. (2010) measurement remains below all published estimates and recent results reach masses only as low as about $3.2 \times 10^{11} M_{\odot}$ (Gibbons et al. 2014).

5.1 Creating and observing mock data sets

We use the self-consistent field method (SCF, Hernquist & Ostriker 1992), which represents the gravitational potential of the disrupting satellite as a basis function expansion, to create a series of N-body simulations designed to reasonably mimic the observed Orphan Stream. The single-component, dark matter only Orphan progenitor is implemented as a Navarro–Frenk–White (NFW, Navarro et al. 1997) distribution with 10^5 particles. The particles are instantiated out to 35 scale radii and so the model’s total mass differs from the virial mass; in the following we report the corresponding virial mass to avoid confusion. All simulations have the same mean density inside the scale radius, which results in tides unbinding them at approximately the same time. This allows the separation of effects due to the time of disruption and passive evolution. The density scaling is set such that the halo with a virial mass of $10^9 M_{\odot}$ has a scale radius of 0.75 kpc although the results are not particularly sensitive to this choice.

We chose the orbit and potential model to be precisely that of Newberg et al. (2010)’s Model 5: that is, an orbit initialized from the phase space coordinate with Heliocentric position $(l, b, R) = (218^{\circ}, 53.5^{\circ}, 28.6 \text{ kpc})$ and Galactocentric velocity $(v_x, v_y, v_z) = (156, 79, 107) \text{ km s}^{-1}$ moving in a logarithmic potential model (Equations 3–5) with the one unspecified parameter v_{halo} set to 73 km s^{-1} . The orbit is integrated backwards in time to find the phase space coordinate of the 3rd apocenter, 4.8 Gyr ago. When the satellite is near apocenter the hosts’ tidal field is at its weakest, so beginning the simulation here minimizes artificial gravitational shocking. After relaxing in isolation the host potential is turned on over 10 internal dynamical times, the particle distribution is inserted, and the satellite is evolved to the present day. We assume that the current position of the progenitor is at the overdensity identified by Grillmair et al. (2015), $l \approx 268.7^{\circ}$, so the simulation ends at that point.

To produce synthetic observations that approximate those of the SMHASH RRL, we first select the particles below the tenth percentile in initial internal binding energy. These are tagged as stars. This simple strategy has been shown to reproduce the observed properties of Local Group dwarf galaxies in semianalytic models (Bullock & Johnston 2005) and create stellar haloes with realistic properties in simulations of Milky Way-like galaxies with cosmological infall (De Lucia & Helmi 2008; Cooper et al. 2010). From this subset we choose at random 30 particles that match the selection criteria used in Sesar et al. (2013), namely Galactic longitude $260^{\circ} > l > 160^{\circ}$, Orphan latitude $4^{\circ} > B > -4^{\circ}$, and Galactic standard of rest velocity $v_{\text{gsr}} > 40 \text{ km s}^{-1}$. Since the particle positions and velocities are precisely known, we introduce ‘observational’ uncertainties by adding a random velocity drawn from a Gaussian of width 15 km s^{-1} to each particle’s heliocentric velocity. Similarly, the selected particles are scattered in heliocentric distance according to the 2.5% relative uncertainty demonstrated in Figure 2. These same values are retained as uncertainties to be fed into the orbit fitting algorithm as well.

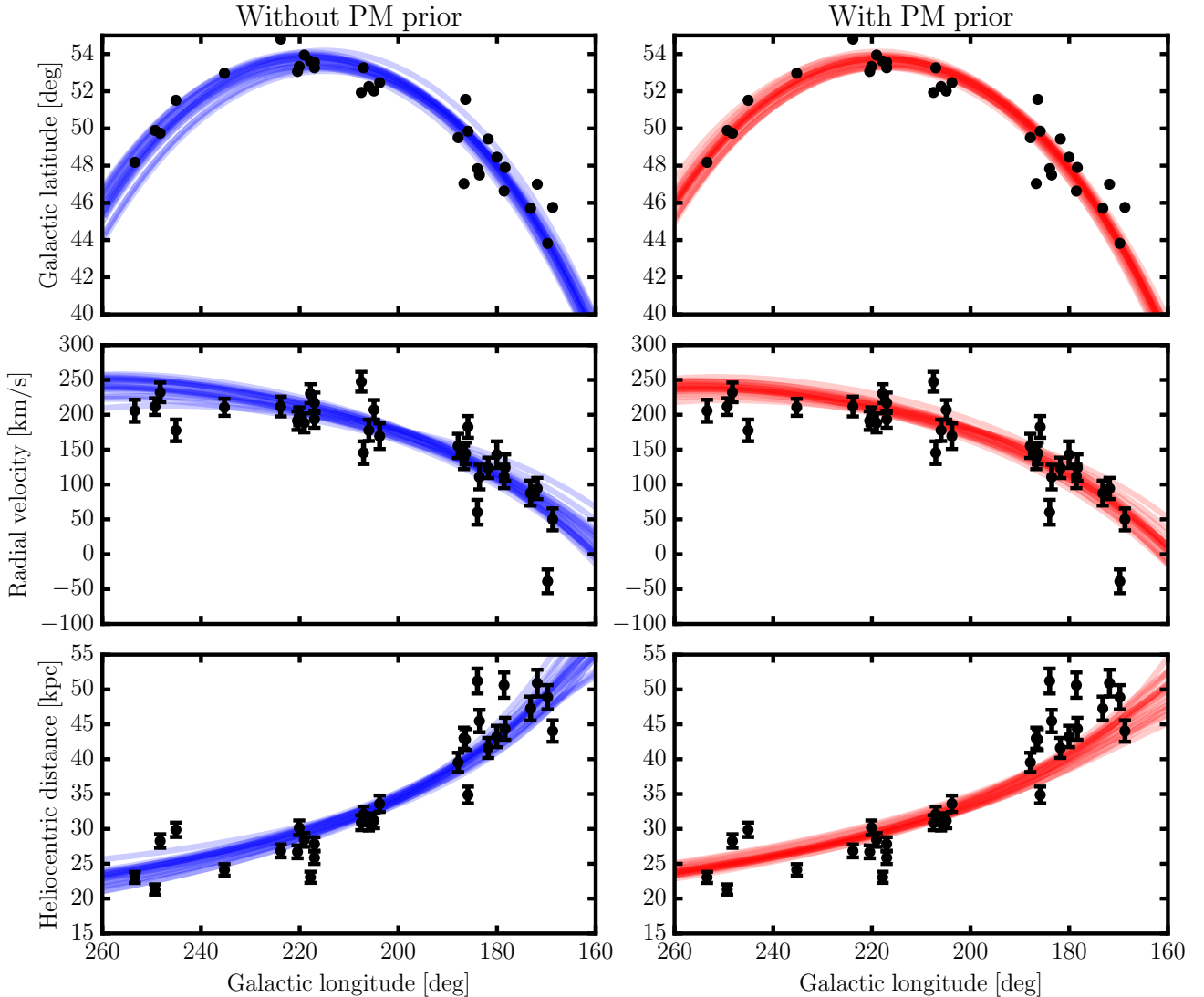


Figure 7. Left: a selection of orbit fits (blue lines) generated from randomly selected samples of the posterior distribution shown in Figure 4, where the proper motion prior is uninformative. Right: the same (red lines), but with samples from the walkers constrained by the observed $\mu_l \cos b$ and μ_b . The former better reproduces the trend of distance with longitude, while the latter slightly improves the match in radial velocity and sky position, especially at $l > 240^\circ$.

5.2 Biases in orbit fitting

The problems associated with assuming stars in a tidal stream follow a single orbit are conceptually simplified when considering the Orphan Stream since we observe only the leading tail. In this case, stars farther from the satellite – towards apocenter – have lower total energy; their individual orbits turn around at smaller Galactocentric radii than the progenitor’s does. Thus, orbits matched to the stream’s path are tracing both the loss of kinetic energy to the gravitational potential as well as an additional loss determined by the total energy gradient of stars along the stream. Since the latter is not modelled in orbit fitting, the potential needs to be deeper at fixed radius to compensate for this ‘extra’ loss, leading to an inflated mass estimate.

Figure 8 illustrates the systematic error in inferred mass introduced by this effect. Despite the fact

that each simulation was run in a potential with $M_{\text{encl}}(60 \text{ kpc}) = 2.7 \times 10^{11} M_\odot$, the median value of the marginalized posterior distributions of v_{halo} generate an estimate ~ 33 per cent more massive. The bias is nearly independent of satellite mass, which matches theoretical expectations (Sanders & Binney 2013). To our knowledge this is the first time that the bias in mass enclosed due to orbit fitting has been quantified in a scenario that replicates an observed system. The magnitude of the effect likely depends on the details of the potential model but the direction should not – the fitting algorithm will always prefer haloes that are more massive than are correct. For this reason we report the value measured for the Milky Way as only an upper limit.

We also note that the already low enclosed mass measurement of Newberg et al. (2010) should also be affected by this systematic error since the approximation is the same despite their different fitting technique. If the magnitude of the

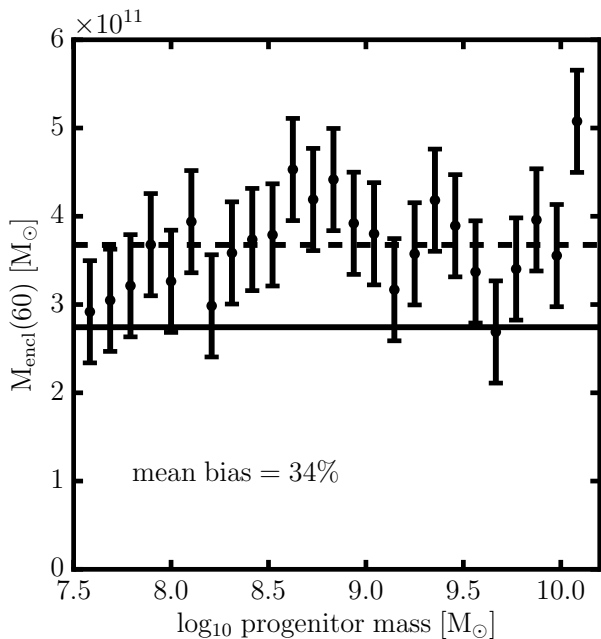


Figure 8. Bias in the best-fitting host halo’s enclosed mass, calculated from v_{halo} , as a function of the initial halo mass of the progenitor satellite. The black horizontal line represents the true value in the model potential, while the points illustrate the posterior distribution of the fitted v_{halo} in the N-body simulations. The dashed line is the mean fitted mass, which is greater than the true value by 34%.

bias is identical then the corrected mass enclosed is approximately $1.8 \times 10^{11} M_{\odot}$, slightly more than half that found by Gibbons et al. (2014). Models with such small enclosed masses may have difficulty matching other observables such as the circular velocity of the Sun.

6 THE ORPHAN PROGENITOR

In the previous section we were concerned primarily with the model parameters that describe the phase space position of the orbits and the shape of the potential. Now we focus on the internal structure of the stream, characterized by the widths δ_B , δ_{v_r} , and δ_{DM} . For a particular progenitor orbit the spatial and velocity scales of the stream stars vary with the satellite-to-host mass ratio as $(m/M)^{1/3}$ (Johnston 1998; Helmi & White 1999; Johnston et al. 2001); therefore the δ_i contain information about the progenitor system. To first order this is the mass when the stars are unbound, however it may be possible to recover the satellite’s central density distribution which also imprints itself on the stream (Errani et al. 2015).

Figure 9 shows the effect of satellite mass on the simulated streams’ structural parameters. In each panel the horizontal blue lines illustrate the values measured from the SMHASH data while the black points show the same quantities found after applying the same orbit fitting algorithm to N-body simulations of varying initial satellite halo masses. The mass range shown, from 3.8×10^7 to $1.2 \times 10^{10} M_{\odot}$, cap-

tures dwarf galaxies from the ultrafaints to a few times less massive than the Small Magellanic Cloud (Guo et al. 2010).

First we consider the stream’s width on the sky, δ_B , plotted in the upper panel. The measured value $\delta_B = 1^{\circ}$ appears at a glance to be most consistent with the lowest-mass simulations, indicating that $M_{\text{Orphan}} \approx 10^8 M_{\odot}$. However, the selection of RR Lyrae stars for spectroscopic follow-up in the SMHASH precursor catalogues is non-uniform and appears to be weighted significantly towards stars that are nearer the stream centre (e.g., of the stars with $2^{\circ} < B < 4^{\circ}$, 3 have spectra and 11 do not). The observed δ_B is therefore unlikely to be representative of the true distribution. An alternative approach is to look at studies of Orphan’s main sequence population; since our synthetic RRL are selected at random from the star particles, they represent any other stellar population just as well under the assumption that Orphan was originally well mixed. Belokurov et al. (2007) found that the stream has a full-width half-max of around 2° , which is comparable to the SMHASH RRL $\delta_B = 1^{\circ}$. However, Sales et al. (2008) showed that the observed stream width may be truncated by confusion with the Galactic background and that streams as wide as 15° could be hidden in the data. We therefore take δ_B as measured in SMHASH as a lower limit on acceptable values in the N-body simulations, indicating $M_{\text{Orphan}} \gtrsim 10^8 M_{\odot}$.

Next, we consider the velocity dispersion δ_{v_r} , shown in the middle panel of Figure 9. It is clear that our model fits cannot reproduce the observed velocity dispersion except in the case of the highest mass progenitors. In fact, the true dispersion is buried by the simulated velocity errors for the lower mass models, resulting in a flat profile across much of the mass range. To obtain the 30 km s^{-1} required to match the δ_{v_r} fit to the (Sesar et al. 2013) velocities would require a satellite of mass $\gtrsim 10^{10} M_{\odot}$. Such a progenitor seems unlikely given Orphan’s luminosity and metallicity as well as the other structural parameters. In addition, Newberg et al. (2010) measured the velocity dispersion of Orphan’s BHB stars and found $\sigma_v = 8 - 13 \text{ km s}^{-1}$ at various points along the stream; similarly, the K-giants surveyed by Casey et al. (2013) have a velocity dispersion of $6.5 \pm 7.0 \text{ km s}^{-1}$. Values in the $5 - 15 \text{ km s}^{-1}$ range are consistent with a wide variety of N-body models. We note that obtaining systemic velocities for RRL requires subtraction of the stars’ atmospheric velocities as they pulsate. The velocity variation of spectral lines over a single cycle can approach 100 km s^{-1} (e.g. Preston 2011), so if even a fraction remains it could explain this discrepancy. Due to this concerns we place lower weight on δ_{v_r} as a constraint and consider it as only an upper limit on progenitor mass.

Finally, the bottom panel of Figure 9 shows the trend of line-of-sight depth in distance modulus, δ_{DM} , as a function of progenitor mass. Of our measurements this dimension provides the most confident constraint on the Orphan progenitor. A line fit to the apparently linear behaviour of the models above $10^9 M_{\odot}$ shows that an initial mass $M_{\text{Orphan}} \approx 3.2 \times 10^9 M_{\odot}$ best reproduces the observed depth of 0.224 mag. At high satellite mass the stream begins fanning out near apocenter due to azimuthal precession of the orbits, leading to larger depths and increased dependence of measured parameters on the selection of simulation particles as RRL.

Taken as a whole, the structure of the stream suggests

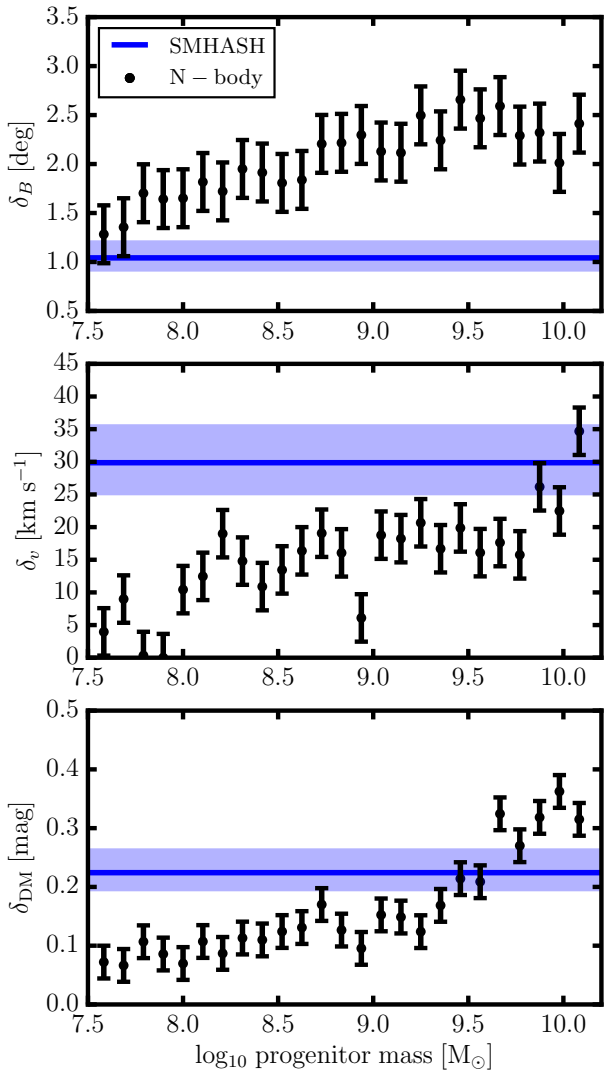


Figure 9. Fitted values of width on the sky (top), velocity dispersion (center), and line-of-sight depth (bottom) for a set of N-body models of the Orphan Stream (black points) as a function of model satellite mass, compared to the same quantities as measured for the SMHASH Orphan data (blue region).

a progenitor with initial halo mass of several times $10^9 M_{\odot}$. That value is in good agreement with the Local Group dwarf spheroidals, who seem to live in haloes in this range (Peñarrubia et al. 2008; Boylan-Kolchin et al. 2012; Fattahi et al. 2016) and provides further evidence that Orphan is indeed a disrupted dwarf spheroidal galaxy. Satellite mass measurements obtained in this way are naturally potential-dependent since the stream structure is sensitive principally to the mass ratio. While the average v_{halo} fit in the N-body models is well matched to that of SMHASH we cannot say with confidence that the bias will be identical. Using any literature value for the Milky Way’s mass will vary this result by less than a factor of 2, surely less than the systematic uncertainty in this simple method.

7 SUMMARY

This work presents *Spitzer Space Telescope* observations of 32 candidate Orphan Stream RR Lyrae stars as part of the *Spitzer* Merger History and Shape of the Galactic Halo (SMHASH) program. Using a theoretical period–luminosity–metallicity relation at $3.6\mu\text{m}$ in conjunction with archival data we have obtained distances to individual stars with 2.5% relative uncertainties, a factor of two better than the previous state of the art. We find that the stream extends to approximately 50 kpc in heliocentric distance within the survey footprint and have resolved its large line-of-sight depth of approximately 8 kpc as it approaches apocenter.

Using a Markov Chain Monte Carlo orbit fitting algorithm, we find that the SMHASH data are consistent with a more massive Milky Way halo than indicated by previous work using same stream and a similar technique. By comparing with N-body simulations of dwarf galaxy tidal disruptions, we find that orbits fit to the available Orphan data are biased to high masses, suggesting that our measurement is an upper limit (and in good agreement with other modern methodologies). While proper motion measurements seem to provide significant leverage on the Milky Way’s halo, our potential model is apparently too rigid to take advantage of the full phase space information. Integrating six-dimensional constraints are a promising avenue for future work.

By examining the structure of the stream – namely its line-of-sight depth, velocity dispersion, and width on the sky – we find that a satellite galaxy with an initial halo mass $M_{\text{Orphan}} \approx 3.2 \times 10^9 M_{\odot}$ best reproduces the SMHASH data. In combination with the integrated luminosity of the stream, this indicates that the progenitor was likely comparable to the Milky Way’s eight classical dwarf spheroidals.

The SMHASH RR Lyrae star distances are fertile ground for further detailed study of the Orphan Stream. The investigations presented here represent only a first step towards understanding this surprisingly complex object. Future work, including implementing sophisticated potential measuring techniques and leveraging additional data from the *Gaia* mission and others, promises to improve our knowledge of the Milky Way and its satellite system.

ACKNOWLEDGEMENTS

DH thanks Peter Stetson, Sheila Kannappan, and Vasily Belokurov for helpful discussions. This work is based on observations made with the *Spitzer Space Telescope*, which is operated by the Jet Propulsion Laboratory, California Institute of Technology under a contract with NASA. DH and KVJ acknowledge support on various aspects of this project from NASA through subcontract JPL 1558281 and ATP grant NNX15AK78G, as well as from the NSF through the grant AST-1614743. The Space Telescope Science Institute (STScI) co-authors acknowledge NASA support through a grant for HST program GO-13443 from STScI, which is operated by the Association of Universities for Research in Astronomy (AURA), Inc., under NASA contract NAS5-26555. DH acknowledges the use of the Shared Research Computing Facility at Columbia University. This work made use of Matplotlib (Hunter 2007), SciPy (Jones et al. 2001), Astropy (Astropy Collaboration et al. 2013), and the Astropy-affiliated Gala package (Price-Whelan 2017).

REFERENCES

- Amorisco N. C., 2015, *MNRAS*, **450**, 575
- Astropy Collaboration et al., 2013, *A&A*, **558**, A33
- Belokurov V., et al., 2006, *ApJ*, **642**, L137
- Belokurov V., et al., 2007, *ApJ*, **658**, 337
- Bersier D., Wood P. R., 2002, *AJ*, **123**, 840
- Bland-Hawthorn J., Gerhard O., 2016, *ARA&A*, **54**, 529
- Bono G., Caputo F., Castellani V., Marconi M., Storm J., 2001, *MNRAS*, **326**, 1183
- Bono G., Caputo F., Castellani V., Marconi M., Storm J., Degl'Innocenti S., 2003, *MNRAS*, **344**, 1097
- Bovy J., et al., 2012, *ApJ*, **759**, 131
- Bovy J., Bahmanyar A., Fritz T. K., Kallivayalil N., 2016, *ApJ*, **833**, 31
- Boylan-Kolchin M., Bullock J. S., Kaplinghat M., 2012, *MNRAS*, **422**, 1203
- Braga V. F., et al., 2015, *ApJ*, **799**, 165
- Bullock J. S., Johnston K. V., 2005, *ApJ*, **635**, 931
- Bullock J. S., Kravtsov A. V., Weinberg D. H., 2001, *ApJ*, **548**, 33
- Cacciari C., Clementini G., 2003, in Alloin D., Gieren W., eds, *Lecture Notes in Physics*, Berlin Springer Verlag Vol. 635, *Stellar Candles for the Extragalactic Distance Scale*. pp 105–122 ([arXiv:astro-ph/0301550](https://arxiv.org/abs/astro-ph/0301550)), doi:10.1007/978-3-540-39882-0_6
- Cardelli J. A., Clayton G. C., Mathis J. S., 1989, *ApJ*, **345**, 245
- Carlin J. L., Majewski S. R., Casetti-Dinescu D. I., Law D. R., Girard T. M., Patterson R. J., 2012, *ApJ*, **744**, 25
- Casey A. R., Da Costa G., Keller S. C., Maunder E., 2013, *ApJ*, **764**, 39
- Catelan M., Pritzl B. J., Smith H. A., 2004, *ApJS*, **154**, 633
- Cohen J., Sesar B., Bahnlolzer S., He K., Kulkarni S. R., Prince T. A., Bellm E., Laher R. R., 2017, preprint, ([arXiv:1710.01276](https://arxiv.org/abs/1710.01276))
- Cooper A. P., et al., 2010, *MNRAS*, **406**, 744
- De Lucia G., Helmi A., 2008, *MNRAS*, **391**, 14
- Drake A. J., et al., 2009, *ApJ*, **696**, 870
- Drake A. J., et al., 2013, *ApJ*, **763**, 32
- Errani R., Peñarrubia J., Tormen G., 2015, *MNRAS*, **449**, L46
- Eyre A., Binney J., 2011, *MNRAS*, **413**, 1852
- Fakhouri O., Ma C.-P., Boylan-Kolchin M., 2010, *MNRAS*, **406**, 2267
- Fattahi A., Navarro J. F., Sawala T., Frenk C. S., Sales L. V., Oman K., Schaller M., Wang J., 2016, preprint, ([arXiv:1607.06479](https://arxiv.org/abs/1607.06479))
- Fazio G. G., et al., 2004, *ApJS*, **154**, 10
- Fiorentino G., et al., 2015, *ApJ*, **798**, L12
- Foreman-Mackey D., 2016, *The Journal of Open Source Software*, **24**
- Foreman-Mackey D., Hogg D. W., Lang D., Goodman J., 2013, *PASP*, **125**, 306
- Freedman W. L., Madore B. F., Scowcroft V., Burns C., Monson A., Persson S. E., Seibert M., Rigby J., 2012, *ApJ*, **758**, 24
- Freeman K., Bland-Hawthorn J., 2002, *ARA&A*, **40**, 487
- Fritz T. K., Kallivayalil N., 2015, *ApJ*, **811**, 123
- Gibbons S. L. J., Belokurov V., Evans N. W., 2014, *MNRAS*, **445**, 3788
- Gibbons S. L. J., Belokurov V., Evans N. W., 2017, *MNRAS*, **464**, 794
- Gillessen S., Eisenhauer F., Fritz T. K., Bartko H., Dodds-Eden K., Pfuhl O., Ott T., Genzel R., 2009, *ApJ*, **707**, L114
- Goodman J., Weare J., 2010, *Comm. App. Math. Comp. Sci.*, **5**, 65
- Grillmair C. J., 2006, *ApJ*, **645**, L37
- Grillmair C. J., Hetherington L., Carlberg R. G., Willman B., 2015, *ApJ*, **812**, L26
- Guo Q., White S., Li C., Boylan-Kolchin M., 2010, *MNRAS*, **404**, 1111
- Helmi A., White S. D. M., 1999, *MNRAS*, **307**, 495
- Hendel D., Johnston K. V., 2015, *MNRAS*, **454**, 2472
- Hernitschek N., et al., 2017, preprint, ([arXiv:1710.09436](https://arxiv.org/abs/1710.09436))
- Hernquist L., 1990, *ApJ*, **356**, 359
- Hernquist L., Ostriker J. P., 1992, *ApJ*, **386**, 375
- Hunter J. D., 2007, *Computing In Science & Engineering*, **9**, 90
- Indebetouw R., et al., 2005, *ApJ*, **619**, 931
- Johnston K. V., 1998, *ApJ*, **495**, 297
- Johnston K. V., Hernquist L., Bolte M., 1996, *ApJ*, **465**, 278
- Johnston K. V., Sackett P. D., Bullock J. S., 2001, *ApJ*, **557**, 137
- Johnston K. V., Bullock J. S., Sharma S., Font A., Robertson B. E., Leitner S. N., 2008, *ApJ*, **689**, 936
- Johnston K., et al., 2013, SMASH: Spitzer Merger History and Shape of the Galactic Halo, Spitzer Proposal
- Jones E., Oliphant T., Peterson P., et al., 2001, *SciPy: Open source scientific tools for Python*, <http://www.scipy.org/>
- Keller S. C., Murphy S., Prior S., DaCosta G., Schmidt B., 2008, *ApJ*, **678**, 851
- Kirby E. N., Cohen J. G., Guhathakurta P., Cheng L., Bullock J. S., Gallazzi A., 2013, *ApJ*, **779**, 102
- Koposov S. E., Rix H.-W., Hogg D. W., 2010, *ApJ*, **712**, 260
- Koposov S. E., et al., 2012, *ApJ*, **750**, 80
- Küpper A. H. W., Balbinot E., Bonaca A., Johnston K. V., Hogg D. W., Kroupa P., Santiago B. X., 2015, *ApJ*, **803**, 80
- Law D. R., Majewski S. R., 2010, *ApJ*, **714**, 229
- Law D. R., Johnston K. V., Majewski S. R., 2005, *ApJ*, **619**, 807
- Law N. M., et al., 2009, *PASP*, **121**, 1395
- Layden A. C., 1994, *AJ*, **108**, 1016
- Longmore A. J., Fernley J. A., Jameson R. F., 1986, *MNRAS*, **220**, 279
- Lux H., Read J. I., Lake G., Johnston K. V., 2013, *MNRAS*, **436**, 2386
- Madore B. F., et al., 2013, *ApJ*, **776**, 135
- Majewski S. R., Skrutskie M. F., Weinberg M. D., Ostheimer J. C., 2003, *ApJ*, **599**, 1082
- Makovoz D., Khan I., 2005, in Shopbell P., Britton M., Ebert R., eds, *Astronomical Society of the Pacific Conference Series* Vol. 347, *Astronomical Data Analysis Software and Systems XIV*. p. 81
- McMillan P. J., 2011, *MNRAS*, **414**, 2446
- Miyamoto M., Nagai R., 1975, *PASJ*, **27**, 533
- Navarro J. F., Frenk C. S., White S. D. M., 1997, *ApJ*, **490**, 493
- Neeley J. R., et al., 2015, *ApJ*, **808**, 11
- Neeley J. R., et al., 2017, *ApJ*, **841**, 84
- Newberg H. J., Willett B. A., Yanny B., Xu Y., 2010, *ApJ*, **711**, 32
- Pawlowski M. S., Pflamm-Altenburg J., Kroupa P., 2012, *MNRAS*, **423**, 1109
- Peñarrubia J., McConnachie A. W., Navarro J. F., 2008, *ApJ*, **672**, 904
- Pearson S., Küpper A. H. W., Johnston K. V., Price-Whelan A. M., 2015, *ApJ*, **799**, 28
- Persson S. E., Madore B. F., Krzemiński W., Freedman W. L., Roth M., Murphy D. C., 2004, *AJ*, **128**, 2239
- Preston G. W., 2011, *AJ*, **141**, 6
- Price-Whelan A. M., 2017, *The Journal of Open Source Software*, **2**
- Price-Whelan A. M., Johnston K. V., 2013, *ApJ*, **778**, L12
- Price-Whelan A. M., Sesar B., Johnston K. V., Rix H.-W., 2016, *ApJ*, **824**, 104
- Rau A., et al., 2009, *PASP*, **121**, 1334
- Saha A., 1985, *ApJ*, **289**, 310
- Sales L. V., et al., 2008, *MNRAS*, **389**, 1391
- Sanders J. L., Binney J., 2013, *MNRAS*, **433**, 1813
- Sanderson R. E., 2016, *ApJ*, **818**, 41
- Sanderson R. E., Helmi A., Hogg D. W., 2015, *ApJ*, **801**, 98
- Schlafly E. F., Finkbeiner D. P., 2011, *ApJ*, **737**, 103

- Schönrich R., Binney J., Dehnen W., 2010, *MNRAS*, **403**, 1829
Scowcroft V., Freedman W. L., Madore B. F., Monson A. J.,
Persson S. E., Seibert M., Rigby J. R., Sturch L., 2011, *ApJ*,
743, 76
Sesar B., et al., 2010, *ApJ*, **708**, 717
Sesar B., et al., 2013, *ApJ*, **776**, 26
Sesar B., et al., 2015, *ApJ*, **809**, 59
Sesar B., Hernitschek N., Dierickx M. I. P., Fardal M. A., Rix
H.-W., 2017, *ApJ*, **844**, L4
Sohn S. T., et al., 2016, *ApJ*, **833**, 235
Stetson P. B., 1987, *PASP*, **99**, 191
Stetson P. B., 1994, *PASP*, **106**, 250
Stokes G. H., Evans J. B., Vighh H. E. M., Shelly F. C., Pearce
E. C., 2000, *Icarus*, **148**, 21
Watkins L. L., et al., 2009, *MNRAS*, **398**, 1757
Werner M. W., et al., 2004, *ApJS*, **154**, 1
White S. D. M., Rees M. J., 1978, *MNRAS*, **183**, 341
Xue X. X., et al., 2008, *ApJ*, **684**, 1143

APPENDIX A: SMHASH LIGHT CURVES

This paper has been typeset from a $\text{\TeX}/\text{\LaTeX}$ file prepared by the author.

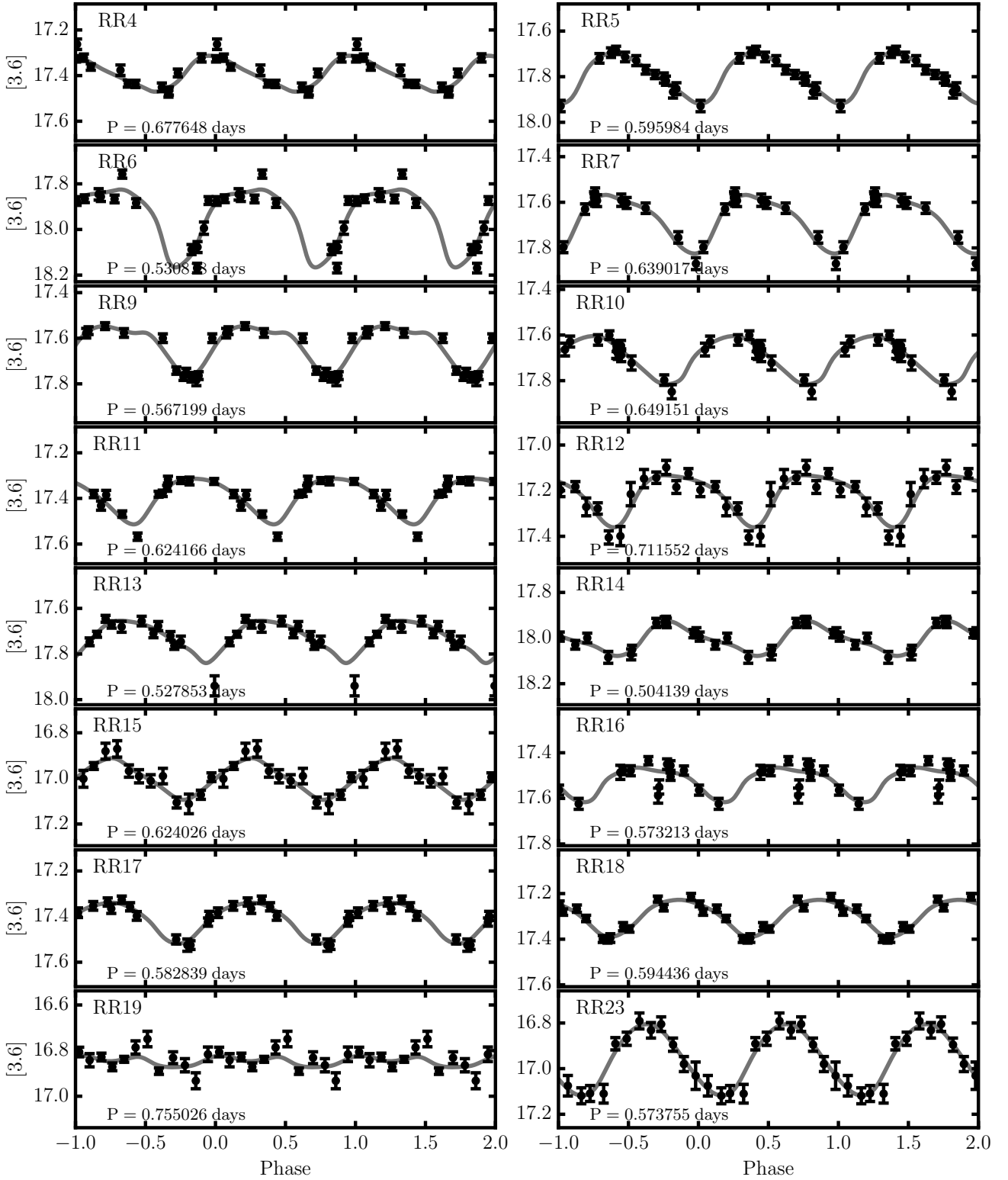


Figure A1. *Spitzer* 3.6 μ m lightcurves of the 32 SMHASH Orphan Stream RR Lyrae star candidates. Each was observed in 12 epochs; the data and fitted lightcurves are repeated through three phase cycles for visual clarity. All stars are shown on the same scale so that amplitude variation is visible. The periods shown were measured from the archival optical survey data (Sesar et al. 2013). RR19 is likely not an RR Lyrae star or a stream member but we include it here for completeness.

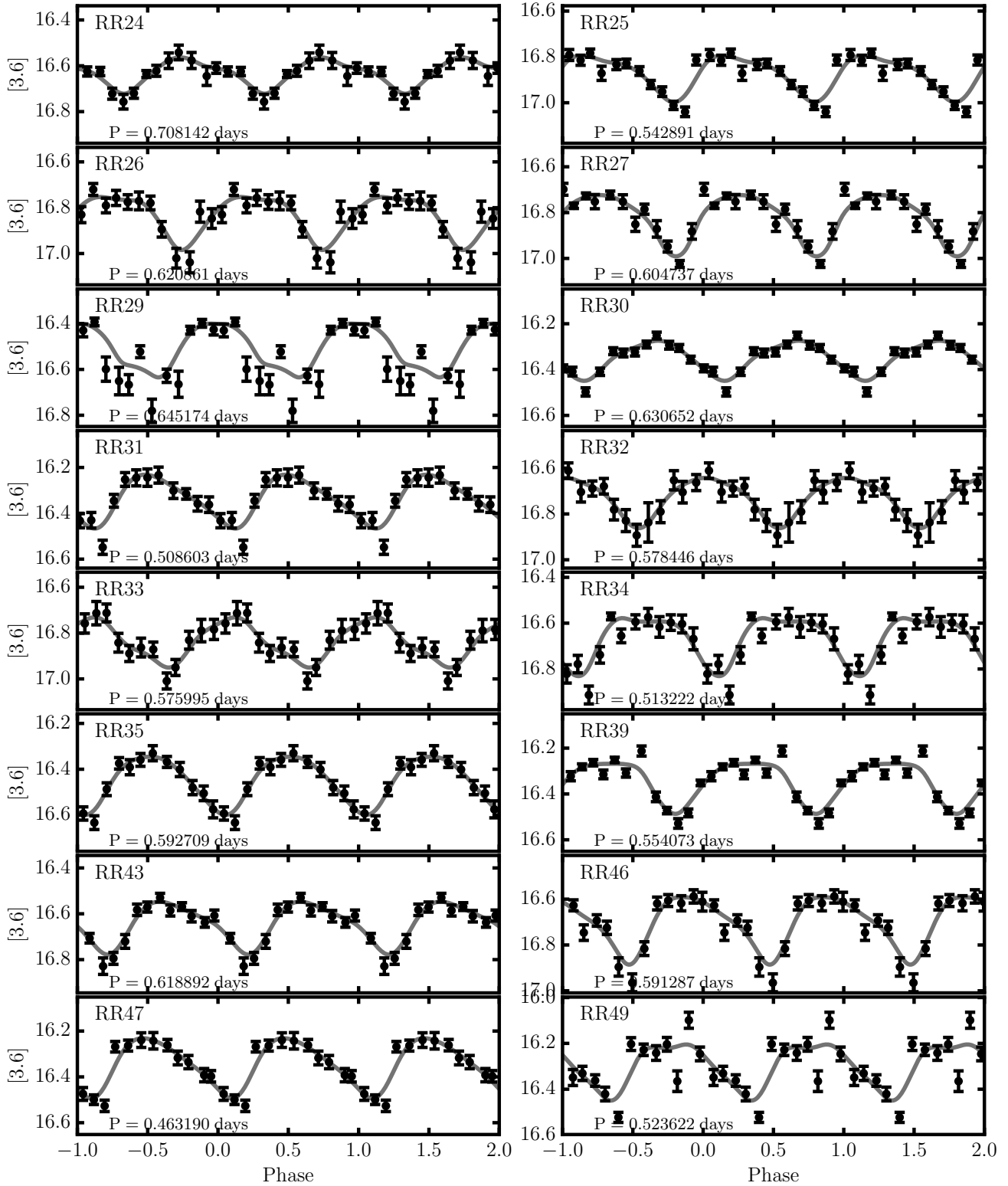


Figure A1. Lightcurves, continued